Mechanical Systems and Signal Processing 243 (2026) 113660

Contents lists available at ScienceDirect

Mechanical Systems and Signal Processing

journal homepage: www.elsevier.com/locate/ymssp

Full length article

Ultrasonic signal decomposition through gradient descent assisted successive parameter estimation

Georgios Sarris *, Michael J.S. Lowe, Peter Huthwaite

Department of Mechanical Engineering, Imperial College London, Exhibition Road, South Kensington, London, SW7 2AZ, United Kingdom

ARTICLE INFO

Communicated by A. Morassi

Keywords:
Signal decomposition
Matching pursuit
Gradient descent
Ultrasonic data compression
Signal processing

ABSTRACT

Accurate decomposition of ultrasonic signals into simple pulses is valuable both for data compression purposes, as well as various medical and engineering applications. This work proposes a matching pursuit (MP) based algorithm that deploys a traditional successive parameter estimation approach, to express ultrasonic signals as sums of Gaussian pulses or chirplets. However, here the MP algorithm is aided by mathematical optimisation (gradient descent), which allows for significantly more precise parameter estimation. Our method is validated on simple input signals, and following its validation, its performance is assessed against cases of increasing complexity. The results not only suggest the accuracy and robustness of our approach, but also show how the proposed method performs well with signals containing strongly overlapping pulses, a challenge for existing methods. Results are also obtained from realistic signals generated through finite element modelling or experimental measurements. Finally, beyond the reconstruction results, we discuss and demonstrate how even complicated signals are well described through only a few parameters, eliminating the need for storing full time traces, allowing for effective ultrasonic data compression.

1. Introduction

Many applications exist where decomposition of a complicated ultrasonic signal into sums of simpler pulses is desirable. For instance, in the area of non-destructive evaluation (NDE), inspection of adhesive bonds [1–3], the estimation of oil thickness in bearings [4–6], the estimation of coating thickness [4,7] and the NDE of batteries [8–12] and composites [13–15] will result in signals containing multiple, partially or sometimes fully overlapping pulses, due to the presence of many thin layers in the component or system being inspected. Also, closely spaced defects in a component and/or complicated geometric features create reflections, which, depending on their exact configuration, may overlap. Examples where this was identified, and potential pulse identification approaches proposed, include the inspection of pipelines using guided waves [16,17] and railway related inspections [18–20]. Decomposition of signals has also been used to aid the characterisation of Lamb waves [21,22].

Apart from the industrial applications discussed above, decomposing ultrasonic signals has proven beneficial in the medical field, with applications in the characterisation of human tissues (liver& spleen [23], skin [24] and bone [25]), and monitoring of arterial health [26–28]. Other areas of interest include seismology [29,30] and even zoology [31].

Over the years, many methods to decompose and reconstruct signals have been derived. A popular group of techniques is those implementing matching pursuit (MP) based sparse decomposition; under those techniques an ultrasonic signal is iteratively expressed as a sum of simple echoes. Those echoes can be Gaussian [32–34], chirplets [35,36] or wavelets [37], amongst others. Modifications

* Corresponding author.
E-mail address: g.sarris18@imperial.ac.uk (G. Sarris).

https://doi.org/10.1016/j.ymssp.2025.113660
Received 15 April 2025; Received in revised form 8 October 2025; Accepted 15 November 2025
Available online 28 November 2025
0888-3270/© 2025 The Authors. Published by Elsevier Ltd. This is an open access article under the CC BY license (http://creativecommons.org/licenses/by/4.0/).

or extensions of the aforementioned method include the use of asymmetric Gaussian pulses [38] and Nagakami functions [39]. Other techniques include those based on linear deconvolution/linear time invariant systems theory [40,41], where the signal is expressed as a convolution between an impulse response and a model echo, as well as applications of the Prony method [34,42], in which the transmitted pulse is used in the deconvolution. Finally, more recent developments in the field use machine learning techniques, with a particular focus on neural networks [43,44].

In this work we propose an alternative method, in which a gradient descent approach is used in conjunction with MP to decompose an ultrasonic signal into a sum of Gaussian pulses or chirplets, with increased accuracy and versatility. Our method extends the well established approach by Lu et al. [35] and Cardoso et al. [33]. In this matching pursuit approach the parameters of a Gaussian pulse or chirplet are estimated such that the pulse is a best fit to the signal which is being deconstructed. The pulse satisfying this condition is subtracted from the signal, and the process is repeated. Once the remainder is sufficiently small, the sum of all pulses can be considered to reproduce the input signal. The parameters defining the Gaussian pulses or the chirplets are estimated successively, with the order of estimation proposed in [33,35] ensuring that the estimation of each parameter becomes independent of the estimation of any subsequent parameters. At this point it is worth noting that this approach leads to a significant reduction in the data needed to store an ultrasonic signal, since a few parameters can fully characterise it. This formed another motivation for this study, especially given the ever increasing amount of data which must be stored and transmitted, both in industrial and medical imaging [33,45,46].

The estimation process described above is based on the characteristics of the maximum of a similarity function. The inherent existence of this function in this method allows us to implement gradient descent to approach the maximum, instead of conventional, grid search approaches. Using gradient descent provides a useful advantage; the value of the similarity function does not rely on the evaluation of the function on pre-determined sets of values, but is rather gradually maximised. This leads to accurate estimations, which do are not limited by any pre-defined grid resolution. Furthermore, significant efficiency gains are possible since many methods to optimise gradient descent approaches are in existence.

In addition to the advantages discussed above, we also address an important issue discussed in [35] and [33], which is the decomposition of signals comprising overlapping pulses of the same, or very similar, central frequency, which is likely to be common in many practical wave applications through NDE and medicine. Instead of using a windowing approach, like in [33,35] a suitable pulse amplitude estimation, based again on gradient descent is presented here, which allows the decomposition of such signals without the need of other inputs, or modifications to the method presented here.

This work focuses on the decomposition of signals into Gaussian echoes, as they are typically used in medical and NDE-related applications. However, our method is easily extended to perform decompositions in chirplets for applications where these are typically encountered, both in engineering, medical or other applications [47–49]. The relevant theory, and some representative examples for chirplet decomposition are presented here as well. This demonstrates the uniformity of our method, and shows how it is straightforward to adapt it to the decomposition of any analytically defined pulse, such as Ricker wavelets, sinc functions and damped sinusoids amongst others, regardless of the number of parameters required to define that pulse.

This paper is organised as follows: Section 2 presents the relevant theory of our method — for completeness and to aid the reader a brief summary of the work on which our method extends is also discussed. Then, following an initial validation of our method on simple signals, Section 3 shows decomposition and reconstruction results of signals of increasing complexity; starting from signals containing non-overlapping pulses, followed by signals comprising overlapping pulses with different central frequencies, where a direct comparison of our results with the results in [33] is presented. The challenging case of multiple, overlapping pulses with the same central frequency is also discussed in the same section. The performance of our method is tested against real-life signals too, and effects of noise on the decomposition process, which was previously a challenge to decompose are investigated. Finally, Section 4 concludes the work.

2. Theory

Many of the pulses typically used in industry and medicine can be approximated as Gaussians. These are expressed as $s(t)$, with

$$s(t) = \Re\left\{A\exp\left[-\alpha(t-\tau)^2 + i(2\pi f(t-\tau)+\phi)\right]\right\}. \tag{1}$$

In (1), A is the amplitude of the pulse, α is the bandwidth factor (which is related to the number of cycles in the signal), τ is the time of arrival of the peak of the pulse, f is the central frequency, ϕ is the phase t is the time and $\Re\{\cdot\}$ denotes the real part of the argument.

Real ultrasonic signals often do not comprise a single pulse, and can have complicated shapes as a result of the superposition of multiple reflections and modes present in them. It has been demonstrated that such ultrasonic signals can be expressed as sums of Gaussian pulses [32]; therefore, we are able to decompose any signal $y(t)$ into a sum of M Gaussian pulses $s_m(t)$, as follows:

$$y(t) = \sum_{m=1}^{M} s_m(t). \tag{2}$$

The focus of this work is the reconstruction of ultrasonic signals into sums of Gaussian pulses. However, there do exist areas where chirps are more commonly encountered — a chirplet, $c(t)$ is expressed as:

$$c(t) = \Re\left\{A_c\exp\left[-\alpha_1(t-\tau_c)^2 + i(2\pi f_c(t-\tau_c)+\phi_c+\alpha_2(t-\tau_c)^2)\right]\right\}, \tag{3}$$

where A_c, α_1, τ_c, f_c, ϕ_c and α_2 are the amplitude, bandwidth factor, central frequency, phase and bandwidth factor of the chirplet respectively.

Our method is not restricted to perform solely with Gaussian pulses; it is possible to extend it to decompose signals into sums of chirplets, in the same way as in Eq. (2), replacing $s_m(t)$ with $c_m(t)$.

In this section, we discuss an existing method which has been used to retrieve the parameters of Gaussian pulses which are subsequently used to reconstruct ultrasonic signals, using a conventional, grid search approach. Then, we present our method, which extends on the existing theory to provide results which do not rely on the fineness of the grid, and that also address other limitations of the method discussed in [33,35]. The relevant theory for extending our method into chirplet deconvolution is also presented.

2.1. Grid search based signal reconstruction — Gaussian pulses

Previous work has shown that the five parameters $(A, \alpha, \tau, f, \phi)$ which fully define a Gaussian pulse, as in Eq. (1), are retrievable using a grid-search based, successive parameter estimation [33]. To achieve this, we start by calculating the continuous wavelet transform (CWT) of the pulse whose parameters are being estimated:

$$\mathrm{CWT} = \int_{-\infty}^{\infty} s(t)\psi^*(t)dt, \tag{4}$$

with respect to the complex conjugate of a wavelet, $\psi^*(t)$, where $\psi(t)$ is given from

$$\psi(t) = \eta \exp\left[-\gamma(t-b)^2 + i(2\pi f_0(t-b)+\theta)\right], \tag{5}$$

with γ, b, f_0 and θ being the bandwidth factor, time of arrival, central frequency and phase of the wavelet respectively, and $\eta = \left(\frac{2\gamma}{\pi}\right)^{\frac{1}{4}}$.

The authors in [33] discuss how a particular order for estimating the five parameters describing the pulse ensures that the estimation of each is independent of the others; first, the value of the |CWT| is numerically calculated using different combinations of b and f_0, where $|\cdot|$ denotes the absolute value. The pair of b and f_0 which maximises the |CWT| is used to estimate τ and f, simply as $\tau = b$ and $f = f_0$. The amplitude of the |CWT| is proportional to the amplitude of $s(t)$ and is therefore used to estimate A. For this step, all other parameters in (5) can be set to arbitrary constants, as they do not affect the prediction of b and f_0.

The next step is to estimate α. The process is similar to before; the |CWT| between $s(t)$ and $\psi^*(t)$ is calculated for different γ values, and the value which maximises the |CWT| is used to estimate α simply from $\alpha = \gamma$. In this step, it is important to set b and f_0 in (5) to the values found in the previous step, while other parameters can be set to arbitrary constants. The same process is repeated for estimating ϕ, this time by varying θ and calculating the $\Re\{\mathrm{CWT}\}$, with ϕ being calculated from $\phi = \theta$ for the value of θ maximising the $\Re\{\mathrm{CWT}\}$, where $\Re\{\cdot\}$ denotes the real part of the argument.

If a signal contains a single Gaussian pulse, that is of the form $s(t)$, the process is completed. Eq. (4) can also take a general signal, $y(t)$ as input — in that case, the result of the process described here is treated as $s_1(t)$ in Eq. (2), and is subtracted from $y(t)$ before the process is repeated with the remainder set to $y(t)$, in the next iteration up until a pre-specified error threshold is met. When this threshold is reached, the initial signal is reconstructed from Eq. (2).

Although this method has certainly shown to provide good results, there are some limitations. Since the method relies in the numerical calculation of the CWT at discrete values, optimal reconstruction of the signal requires that the true value which is to be retrieved exists in the grid on which the CWT is calculated. Therefore, the proximity of the estimated parameter to the true value is a function of the fineness of the grid. This can be mitigated by sufficiently fine grids, at a growing computational and temporal cost. In addition, the authors discuss how a windowing algorithm is required to separate the maxima in the CWT plot during the simultaneous prediction of τ and f, and how overlapping pulses of the same or close central frequencies become increasingly complicated to decompose.

2.2. Gradient descent assisted signal reconstruction — Gaussian pulses

In this work, we propose the use of a gradient descent approach to estimate the parameters of interest, rather than using a grid search approach. Gradient descent is an optimisation algorithm that iteratively adjusts a variable in the direction of the steepest decrease of an error function's slope (negative gradient), until this error function reaches a minimum.

While global optimisation algorithms, such as particle swarm optimisation (PSO), could also be used for this parameter search, a gradient descent approach was selected for two reasons. Firstly, the analytical differentiability of the CWT (or the equivalent transform from any decomposition pulse of choice) allows for the precise computation of the gradient at each step, as shown in Appendix. Secondly, when initialised near the global maximum via a coarse grid search, this method offers rapid convergence to a precise parameter estimate. While this initialisation is not generally possible, we later discuss how we have achieved this in our work. PSO or genetic algorithms on the other hand, would require evaluating the CWT function for many candidate solutions at every single iteration, making them significantly more computationally expensive. Moreover, since the parameter spaces are smooth and differentiable, the additional global search capability of heuristic methods is not required in this context.

Since the process for estimating any parameter in the pulse involves maximising either the |CWT| or the $\Re\{\mathrm{CWT}\}$, we can directly use the CWT as the error function. Since the error function needs to be maximised instead of minimised, steps need to be taken in the positive direction of the gradient.

For each of b, f_0, γ and θ (and hence, τ, f, α and ϕ), gradient descent is implemented as follows:

$$b^{j+1} = b^j + q_b \frac{\partial |\mathrm{CWT}|}{\partial b}\bigg|_{b=b^j}, \tag{6}$$

$$f_0^{j+1} = f_0^j + q_{f_0} \frac{\partial |\mathrm{CWT}|}{\partial f_0}\bigg|_{f_0=f_0^j}, \tag{7}$$

$$\gamma^{j+1} = \gamma^j + q_\gamma \frac{\partial |\mathrm{CWT}|}{\partial \gamma}\bigg|_{\substack{b=\tau,\ f_0=f,\\ \gamma=\gamma^j}}, \tag{8}$$

$$\theta^{j+1} = \theta^j + q_\theta \frac{\partial \Re\{\mathrm{CWT}\}}{\partial \theta}\bigg|_{\substack{b=\tau,\ f_0=f,\\ \gamma=\alpha,\ \theta=\theta^j}}. \tag{9}$$

where the superscript j denotes the value of the variable at the jth iteration, and q is the step size, also commonly referred to as the learning rate in gradient descent applications. This step is not necessarily the same across (6) and (9), and therefore the subscripts in q denote the step taken to implement gradient descent for the variable in their subscript. There are two options to selecting the step size. If a fixed step is selected, we have found that it should be at most 2–3 orders of magnitude smaller than the order of magnitude of the parameter being estimated. Selecting a smaller step size reduces the possibility of any convergence instabilities but also decreases the rate of convergence. However, the authors recommend the use of optimisation methods, such as the Adaptive Moment Estimation (ADAM) algorithm, which adapt the step size for each parameter independently based on its recent past updates, ensuring smooth and often quicker convergence.

The derivatives in Eqs. (6)–(9) are given from

$$\frac{\partial |\mathrm{CWT}|}{\partial b} = \Re\left\{ \frac{|\mathrm{CWT}|}{\mathrm{CWT}} \int_{-\infty}^{\infty} [2\gamma(t-b) + 2\pi i f_0] s(t)\psi^*(t) dt \right\}, \tag{10}$$

$$\frac{\partial |\mathrm{CWT}|}{\partial f_0} = \Re\left\{ -2\pi i \frac{|\mathrm{CWT}|}{\mathrm{CWT}} \int_{-\infty}^{\infty} (t-b) s(t)\psi^*(t) dt \right\}, \tag{11}$$

$$\frac{\partial |\mathrm{CWT}|}{\partial \gamma} = \Re\left\{ -\frac{|\mathrm{CWT}|}{\mathrm{CWT}} \int_{-\infty}^{\infty} \left[\frac{1}{4\gamma} - (t-b)^2 \right] s(t)\psi^*(t) dt \right\}, \tag{12}$$

$$\frac{\partial \Re\{\mathrm{CWT}\}}{\partial \theta} = \Re\{i\mathrm{CWT}\}. \tag{13}$$

respectively. More details about how these expressions were derived are given in Appendix.

The final parameter which needs to be estimated is the amplitude, A. In previous work, A was estimated from the amplitude of the |CWT|, when that was calculated for different b and f_0 values. However, the authors in [33] discuss how applying their approach becomes increasingly difficult with signals containing multiple overlapping pulses, especially when the pulses have the same central frequency. In general, the |CWT| diagram can be thought of as the time–frequency representation of the signal; the amplitude of the |CWT| is an indication as to whether the signal carries any energy at each time and frequency combination. In cases of strongly overlapping pulses with the same central frequency, the peak value of the |CWT| is a result of the superposition of the contributions of each pulse of the signal in the |CWT|, and those contributions happen at the same (or nearby) (b, f_0) locations. Therefore, when decomposing such signals, one can no longer use the |CWT| to estimate the amplitude of each pulse, as the peak of the |CWT| is no longer proportional to the peak of each pulse. Errors in estimating the correct arrival time and central frequency may arise too, as the peak of the |CWT| is no longer necessarily at the arrival time or central frequency of each of the pulses.

To mitigate this, we have again used a gradient descent approach, but with the error function here being the L_2 norm:

$$L_2(B) = \sum_{k=1}^{n} \left\{ y(t_k) - \Re\left\{ B \exp\left[-\gamma(t_k-b)^2 + i(2\pi f_0(t_k-b) + \theta) \right] \right\} \right\}^2, \tag{14}$$

where t_k is the kth timestep, and n is the number of timesteps in $s(t)$. In this equation, the b, f_0, γ and θ values to be used are the converged values of those variables, obtained using Eqs. (6)–(9).

Then, the estimate value of A is obtained from

$$B^{j+1} = B^j - q_B \frac{\partial L_2}{\partial B}\bigg|_{\substack{b=\tau,\ f_0=f,\ \gamma=\alpha,\\ \theta=\phi,\ B=B^j}}, \tag{15}$$

where q_B is the step chosen for applying gradient descent to predict B. We note the use of a minus sign in the equation above, since L_2 is to be minimised. The derivative term in Eq. (15) can be calculated analytically or numerically. For the numerical calculation, this is achieved by choosing two values of B and calculating $L_2(B)$ for those. Then, the equation can be applied for $j = 3$ onwards. Once this process is completed, the amplitude of $s(t)$ is given simply from $A = B$.

While gradient descent is certainly a versatile optimisation tool, there is one drawback of this method that can hinder the optimisation process presented here — it is well known that gradient descent is prone to converging to local instead of global extrema, if the former exist in the error function. In our case, this makes the choice of $b^j, f_0^j, \gamma^j, \theta^j$ and B^j for $j = 1$ very important. While there are methods for improving the likelihood of gradient descent converging to the global minimum [50–54], a simple solution to this issue is to initialise the process at a point close to the global extremum. Generally, this is not known a priori and is therefore infeasible, however, here we propose the use of the grid search approach in [32,33] to provide us with the starting point for estimations. The starting point acts as a guide, and therefore, in the interest of computational efficiency, we propose searching

coarsely spaced grids for b and f_0, and coarsely spaced lists for γ and θ, to identify the starting points. In terms of B, a suitable starting point is the peak of the absolute value of the signal being reconstructed, at each iteration.

Having presented all relevant equations, below we describe how a general signal, $y(t)$, is decomposed into a sum of M Gaussian pulses, as per Eq. (2), using our method. Fig. 1 shows a summary of the decomposition process schematically.

- **Step 1 — estimating τ and f :** Start by creating a coarse grid of b and f_0 values, and calculate the |CWT| on the points of the grid. During the calculation of the CWT, all other variables besides b and f_0 can be set to arbitrary values since they do not affect the prediction process. Find the (b, f_0) pair which maximises the |CWT|, and set those to b^1 and f_0^1 in Eqs. (6) and (7) respectively. Apply gradient descent using the aforementioned equations until convergence. Convergence here can be quantified by calculating the relative change of the variable between two consecutive iterations and comparing it to a pre-determined value. Once the relative change is sufficiently small, no more iterations are required. What is deemed sufficient is application specific. It is worth noting here that the initial grid and subsequent analysis may also be constructed using suitable dimensionless parameters. This also applies in the gradient descent initialisation and implementation in all subsequent steps presented here.
  Once convergence is achieved, set τ and f to the latest value of b^j and f_0^j respectively. In all subsequent steps, use those values when computing $\psi(t)$.
- **Step 2 — estimating α:** The estimation of α (through γ) is a one-dimensional problem, hence only a one dimensional list of different γ values needs to be defined. Calculate the |CWT| for each of the γ values, and set γ^1 to the value in the list which maximises the |CWT|. As mentioned above, in the calculation of the CWT here, we need to set the b and f_0 values to those found in the previous step, while θ and B can be set to arbitrary values. Apply Eq. (8) until convergence, and set α equal to the converged value of γ. In all subsequent steps, use this γ value when computing $\psi(t)$.
- **Step 3 — estimating ϕ:** Estimating ϕ (through θ) is again a one dimensional problem, therefore, an analogous process to that described in Step 2 is repeated; create a list of θ values, calculate the $\Re\{\text{CWT}\}$ for each of the θ values, and set θ to the value in the list which maximises the $\Re\{\text{CWT}\}$. Similarly to before, when calculating the CWT, b, f_0 and γ need to be set to the values found in the two previous steps. The list of possible θ values only needs to contain values $\in [0, 2\pi)$. Apply Eq. (9) until convergence. Then, ϕ is equal to the converged θ value. In the next and final step, use this θ value when computing $\psi(t)$.
- **Step 4 — estimating A :** The last decomposition step is to estimate the amplitude of $s_m(t)$. As discussed above, the minimisation of the L_2 norm instead of the maximisation of the |CWT| is used for the amplitude estimation.
  Start by evaluating Eq. (14) for two different but close B values. A good estimate for those values is to select them to be similar to the amplitude of the signal being decomposed. Based on those values, numerically calculate the derivative in Eq. (15), and apply this equation iteratively, from $j = 3$ onwards. Once convergence is achieved, set A to the converged value of B. Again, while applying Eq. (14), b, f_0, γ and θ need to be set to the values found in Steps 1–3.
- **Step 5 — subtraction:** Now all parameters required to construct $s_m(t)$ have been calculated. Apply those to Eq. (1), to compute $s_m(t)$, and calculate the residual, $r(t) = y(t) - s_m(t)$. Steps 1-5 can be repeated, with $r(t)$ as the input signal for the next iteration as shown schematically in Fig. 1, up until a pre-defined error threshold is met, i.e. up until $r(t)$ becomes sufficiently small. A typical error metric which can be used at each iteration is the relative energy threshold, E. With this metric, the iterative process stops when

$$E = \frac{\sum_{k=1}^{n} r^2(t_k)}{\sum_{k=1}^{n} y_0^2(t_k)} < \epsilon, \tag{16}$$

  where ϵ is the error threshold. E is calculated based on a comparison of $r(t)$ with the initial input signal $y_0(t)$. This new notation for the initial input signal is introduced to avoid confusion with $y(t)$, since, after the first iteration, we are working with the residual from previous iteration and not the initial input signal, i.e. $r(t)$ effectively replaces $y(t)$ at the beginning of every iteration after the first. Typical values of ϵ are between 0.1%–1%, but its selection depends on the required quality of the results.
- **Step 6 — reconstruction:** Having met the error threshold in Step 5, we are now ready to reconstruct the input signal. Assuming steps 1–5 have been repeated M times, Eq. (2) is used to estimate $y(t)$ from a sum of M Gaussian pulses.

In Steps 1–3, we discuss how the estimation of the starting point is achieved by maximising a component of the CWT based on a grid/list search approach. Therefore, it is necessary to ensure that the value being predicted is within the search bounds. While we realise that it is not possible to know this a priori, a large upper bound (larger than the anticipated value of the parameter being estimated) of the list or grid ensures that the starting point of the gradient descent algorithm is found somewhere close to the true value being estimated. Again, this does not generate additional computational cost, because the grid or list are coarsely populated and only serve the purpose of initialising the process described by Eqs. (7)–(9).

2.3. Grid search based signal reconstruction — Chirplets

The focus of this work is the reconstruction of ultrasonic signals through their expression as sums of Gaussian pulses, with the underlying assumption being that the central frequency of the signal remains constant with time. It is, however, straightforward to extend our gradient descent assisted method for expressing signals into sums of chirplets instead. The process of retrieving the

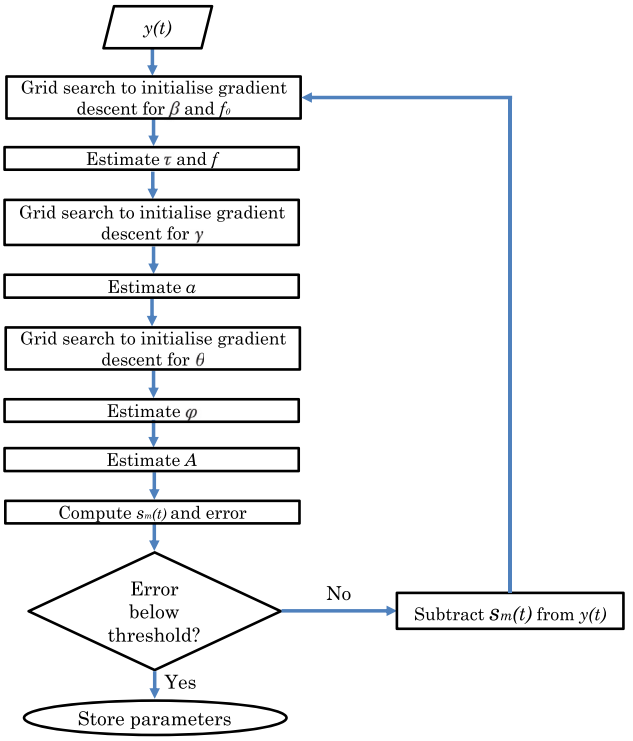


Fig. 1. Flowchart showing a summary of the signal reconstruction process, for decomposing an input signal $y(t)$ into a sum of Gaussian pulses.

parameters defining a chirplet is very similar to before — first, the chirplet transform (CT) of chirplet, whose parameters are being estimated, is calculated with respect to a chirplet kernel:

$$\mathrm{CT} = \int_{-\infty}^{\infty} c(t)\chi^*(t)dt, \tag{17}$$

where the chirplet kernel, $\chi(t)$ is given by

$$\chi(t) = \eta_c \exp\left[-\gamma_1(t-b_c)^2 + i\left(2\pi f_{0_c}(t-b_c) + \theta_c + \gamma_2(t-b_c)^2\right)\right]. \tag{18}$$

In the equation above, γ_1, b_c, f_{0_c}, θ and γ_2 are the bandwidth factor, arrival time, central frequency, phase and chirp rate of the chirplet kernel respectively, and $\eta_c = \left(\frac{2\gamma_1}{\pi}\right)^{0.25}$.

In an extension of the work in [33], the authors in [35] present how an analogous successive parameter estimation retrieves the parameters needed to reconstruct $c(t)$. The method is the same as discussed in Section 2.1; first τ_c and f_c are estimated simultaneously via maximising the |CT|, and $\tau_c = b_c$ and $f_c = f_{0_c}$ for the (b_c, f_{0_c}) pair which maximises the |CT|. A_c is found from the maximum value of the |CT|. This is proportional to the amplitude of the echo being reconstructed. Then α_2 is estimated again through maximising the |CT|, having set b_c and f_{0_c} to the values found before when calculating the |CT|, and $\alpha_2 = \gamma_2$ for the γ_2 where the maximum occurs. Next is α_1, with $\alpha_1 = \gamma_1$ for the γ_1 value which maximises the |CT|, when the other variables in the calculation of the |CT| are set to the values found above. Finally, ϕ_c is estimated from $\phi_c = \theta_c$ for the θ value yielding a maximum for the $\Re\{\mathrm{CT}\}$, once the CT is calculated with all other parameters set to the values found above.

2.4. Gradient descent assisted signal reconstruction — Chirplets

Instead of a grid search approach we are again able to implement a gradient descent approach for decomposition into chirplets; for each of the variables being estimated, gradient descent is implemented as follows:

$$b_c^{j+1} = b_c^j + q_{b_c}\left.\frac{\partial|\mathrm{CT}|}{\partial b_c}\right|_{b_c=b_c^j}, \tag{19}$$

$$f_{0_c}^{j+1} = f_{0_c}^j + q_{f_{0_c}}\left.\frac{\partial|\mathrm{CT}|}{\partial f_{0_c}}\right|_{f_{0_c}=f_{0_c}^j}, \tag{20}$$

$$\gamma_{2_c}^{j+1} = \gamma_{2_c}^j + q_{\gamma_{2_c}}\left.\frac{\partial|\mathrm{CT}|}{\partial \gamma_{2_c}}\right|_{\substack{b_c=\tau_c,\ f_{0_c}=f_c,\\ \gamma_{2_c}=\gamma_{2_c}^j}}, \tag{21}$$

$$\gamma_{1_c}^{j+1} = \gamma_{1_c}^{j} + q_{\gamma_{1_c}} \frac{\partial |\mathrm{CT}|}{\partial \gamma_{1_c}}\bigg|_{\substack{b_c=\tau_c,\ f_{0_c}=f_c,\\ \gamma_2=\alpha_2,\ \gamma_1=\gamma_1^j}}, \tag{22}$$

$$\theta_c^{j+1} = \theta_c^{j} + q_{\theta_c} \frac{\partial \Re\{\mathrm{CT}\}}{\partial \theta_c}\bigg|_{\substack{b_c=\tau_c,\ f_{0_c}=f_c,\ \gamma_2=\alpha_2,\\ \gamma_1=\alpha_1,\ \theta_c=\theta_c^j}}. \tag{23}$$

The derivative terms in Eqs. (19)–(23) are given from:

$$\frac{\partial |\mathrm{CT}|}{\partial b_c} = \Re\left\{ 2\frac{|\mathrm{CT}|}{\mathrm{CT}} \int_{-\infty}^{\infty} [\gamma_1(t-b_c) + i\pi f_{0_c} + \gamma_2(t-b_c)] s(t)\chi^*(t)dt \right\}, \tag{24}$$

$$\frac{\partial |\mathrm{CT}|}{\partial f_{0_c}} = \Re\left\{ -2\pi i \frac{|\mathrm{CT}|}{\mathrm{CT}} \int_{-\infty}^{\infty} (t-b_c) s(t)\chi^*(t)dt \right\}, \tag{25}$$

$$\frac{\partial |\mathrm{CT}|}{\partial \gamma_2} = \Re\left\{ -i \frac{|\mathrm{CT}|}{\mathrm{CT}} \int_{-\infty}^{\infty} (t-b_c)^2 s(t)\chi^*(t)dt \right\}, \tag{26}$$

$$\frac{\partial |\mathrm{CT}|}{\partial \gamma_1} = \Re\left\{ \frac{|\mathrm{CT}|}{\mathrm{CT}} \int_{-\infty}^{\infty} \left[\frac{1}{4\gamma_1} - (t-b_c)^2 \right] s(t)\chi^*(t)dt \right\}, \tag{27}$$

$$\frac{\partial \Re\{\mathrm{CT}\}}{\partial \theta_c} = \Re\{-i\mathrm{CT}\}. \tag{28}$$

More details on how the derivatives terms were calculated are given in Appendix. In the equations above, the subscript of each q refers to the variable being updated, and the value represents the size of the gradient descent step for updating that variable.

Finally, similarly to the deconstruction into Gaussian pulses, the amplitude A_c is estimated from

$$B_c^{j+1} = B_c^{j} - q_{B_c} \frac{\partial L_{2_c}}{\partial B_c}\bigg|_{\substack{b_c=\tau_c,\ f_{0_c}=f_c,\ \gamma_2=\alpha_2,\\ \gamma_1=\alpha_1,\ \theta_c=\phi_c, B_c=B_c^j}}, \tag{29}$$

where q_{B_c} is the step chosen for applying gradient descent to predict B_c, and the L_2 norm with the respect to the chirplet, L_{2_c} is calculated from:

$$L_{2_c}(B_c) = \sum_{k=1}^{n} \left\{ y(t_k) - \Re\left\{ B_c \exp\left[-\gamma_1(t_k-b_c)^2 + i\left(2\pi f_c(t_k-b) + \theta + \gamma_2(t-b)^2\right)\right]\right\}\right\}^2, \tag{30}$$

with the values of b_c, f_c, γ_2, γ_1 and θ being set to their respective converged value calculated using Eq. (19)–(23) respectively. The derivative term in Eq. (29) can be calculated analytically or numerically. For the numerical case this is achieved by choosing two values of B_c and calculating $L_2(B_c)$ for those. Then, the equation can be applied for $j = 3$ onwards. Once this processed is completed, the amplitude of $s(t)$ is given simply from $A_c = B_c$.

The required steps to estimate the parameters of $c_m(t)$ are nearly the same as those described in Section 2.2, with the sole difference that γ_2 needs to be estimated here too. First, b_c and f_{0_c} are estimated simultaneously, followed by γ_2, then γ_1, θ and finally B_c. As described in Section 2.2, each parameter estimation is initialised using a suitable grid search approach, and finalised using gradient descent according to Eqs. (19)–(29). Then, by using $\tau_c = b_c$, $\alpha_2 = \gamma_2$, $\alpha_1 = \gamma_1$, $\phi_c = \theta_c$, and $A_c = B_c$, $c_m(t)$ is found.

If the input signal contains a single echo of the form of $c(t)$, the process is completed. For arbitrary input signals, E (or any other suitable error metric) is again calculated with $r(t) = y(t) - c_m(t)$. Similarly to before, the process is repeated with the residual signal as the input to the next iteration, until the pre-defined error metric is sufficiently small. Once this is achieved, the parameters estimated at each step are stored, and the initial input signal is found from Eq. (2), replacing $s_m(t)$ with $c_m(t)$.

3. Results & discussion

In this section we present reconstructions of signals of increasing complexity. To validate our method, we initially present decomposition and reconstruction results of signals containing a single pulse, whose input parameters are known, to investigate the proximity of the estimated parameters to the corresponding known quantities of the input. Following this validation, we present reconstructions of signals containing multiple pulses, examining both cases of non-overlapping and overlapping pulses. We also examine the challenging case of signals with overlapping pulses with the same central frequency, which was previously thought to have been either very difficult to decompose or required additional manipulation of the CWT or the CT of the signal [33,35]. Finally, we demonstrate the performance of our method on realistic signals; we present the decomposition results of one signal generated via finite-element (FE) modelling and two signals from a real, experimental measurements.

3.1. Single pulse

To validate our method, we attempted to decompose and reconstruct signals containing a single Gaussian pulse or chirplet; since such signals comprise a sole pulse, the parameters which define them are known and therefore, we can assess how well our method is able to estimate those parameters. Also, given that the input signals comprise a single pulse or chirplet, $M = 1$ in Eq. (2), i.e. only a single $s(t)$ or $c(t)$ fully characterises the input signal. Fig. 2 shows a comparison between four input signals, two Gaussian and two chirplets, and their reconstruction using our method.

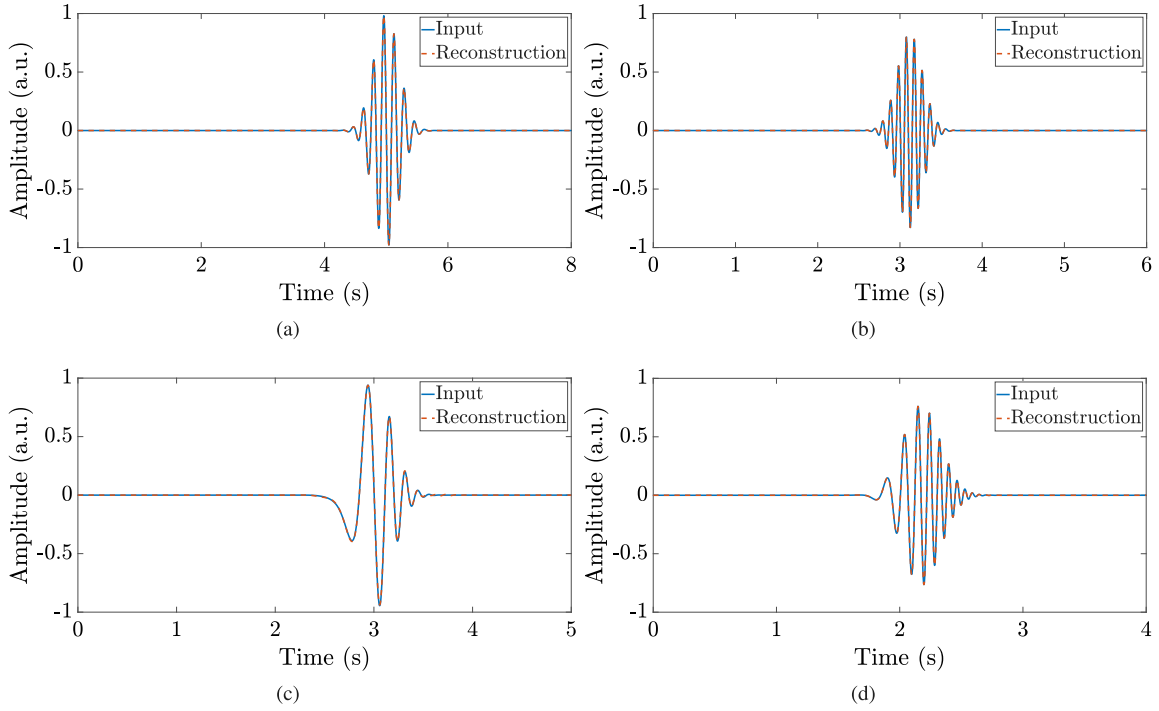


Fig. 2. Examples of input signals, comprising a single pulse, and their reconstructions. In (a) and (b) the input is a Gaussian pulse, with two different sets of parameters (Table 1), while in (c) and (d), a chirplet with again two different sets of parameters (Table 2).

Table 1
Comparison between the input and estimated parameters of the Gaussian signals shown in Fig. 2(a)–(b).

Parameter	A	τ	f	α	ϕ
Input parameters [Fig. 2(a)]	1	5	6	12	1.5
Estimated parameters [Fig. 2(a)]	1.00	5.00	6.00	12.00	1.50
Input parameters [Fig. 2(b)]	0.83	3.12	10.38	21.34	1.69
Estimated parameters [Fig. 2(b)]	0.83	3.12	10.38	21.34	1.69

Table 2
Comparison between the input and estimated parameters of the chirplet signals shown in Fig. 2(c)–(d).

Parameter	A_c	τ_c	f_c	α_2	α_1	ϕ_c
Input parameters [Fig. 2(c)]	1	3	4	30	16	2
Estimated parameters [Fig. 2(c)]	1.000	3.000	4.002	29.974	15.998	2.014
Input parameters [Fig. 2(d)]	0.772	2.175	10.380	52.170	21.341	1.692
Estimated parameters [Fig. 2(d)]	0.772	2.175	10.381	52.143	21.341	1.692

Visually, a very good match is observed between the input pulses and the reconstruction — in all four cases, the reconstructed pulse follows the shape of the input pulse very closely. To quantify the degree of the matching, Tables 1–2 show a comparison between the input and estimated parameters for each pulse.

As shown in Tables 1–2, the match observed in Figs. 2(a)–(d) is not only visual, but all parameters have been predicted precisely or with very small errors. This is regardless of the amplitude, central frequency, arrival time, attenuation, phase and chirp rate which were selected to generate them. Any small errors observed are attributed to insufficient convergence of the parameter being estimated during the gradient descent process — if required, the relevant q value, or the number of iterations completed, can be adjusted to achieve an even better estimation.

The four example signals reconstructed here provide useful initial confirmation of our method; since we are able to accurately retrieve the parameters defining all input pulses, this shows that our method is performing well and as intended. The performance does not differ between Gaussian and chirplet decomposition either. Therefore, for brevity, and since the focus of our work is Gaussian pulses, results presented in subsequent sections will focus on the use of Gaussian pulses, without loss of generality.

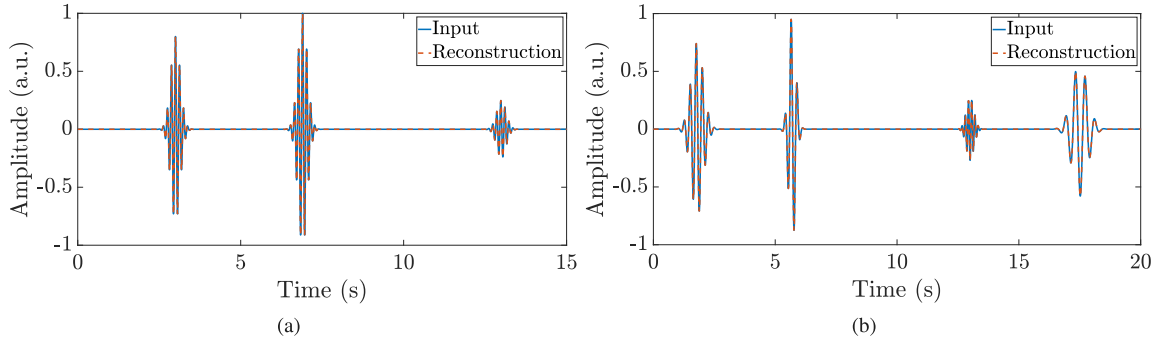


Fig. 3. Examples of input signals, comprising multiple, non overlapping pulses, and their reconstructions. In (a) the signal contains three pulses with the same central frequency, but different amplitudes, phases and arrival times (similar to signals obtained from NDE measurements), while in (b), all parameters of the four pulses in the signal are different between the pulses.

3.2. Multi pulse

Having validated our method using the simple, single pulse signals, we present reconstruction results for more complicated cases, where signals contain more than one pulse.

3.2.1. Non-overlapping pulses

For the case of a signal containing multiple, non overlapping pulses, we have examined two cases. One where all pulses in the signal have the same central frequency, but differ in arrival time, amplitude and length, and a more general case, where all parameters differ between the pulses. The latter is a more general case, but the former (multiple, similar pulses) more realistic, especially in NDE applications where signals often contain ultrasonic reflections from many geometrical features of a component being inspected. The results are shown in Fig. 3.

For both cases presented in Fig. 3, the reconstruction results are accurate — all pulses have been reconstructed correctly. This is true for both the case in Fig. 3(a), where the pulses are copies of each other, simply arriving at different points in time and with different amplitudes, and in Fig. 3(b) where the pulses in the signal differ in all parameters. This demonstrates both that our method is not sensitive to the number of pulses in $y(t)$, but also, that there can exist large variability in the parameters of the echo being estimated in each iteration with respect to the other echoes in the signal, without the latter adversely affecting the estimation process.

3.2.2. Overlapping pulses

When concerned with a single-pulse signal, or multiple well-separated pulses, conventional windowing methods can be used to extract those, and the characteristics of each are retrievable using suitable signal processing methods. Extraction via windowing though is not possible when working with signals containing overlapping pulses, since the start and end points of each pulse are no longer visible in the time trace of the signal. Here, we demonstrate this capability using our method to decompose such signals.

We start by examining a case of two partially overlapping pulses whose parameters differ from each other — the key difference here being that they do not have the same central frequency. Previously, we have discussed how our gradient descent assisted approach yields better results compared with the traditional grid search approaches; to showcase this, we have replicated the signal reconstructed in [33], to directly compare our reconstruction to what was achieved in previous work. The input signal, and our reconstruction are shown in Fig. 4. The input signal, $y(t)$ was reconstructed as a sum of two Gaussian pulses, i.e. by using Eq. (2), $y(t) = s_1(t) + s_2(t)$. In the same figure, we are showing how $s_1(t)$ and $s_2(t)$ compare with the two pulses summed to create the input signal.

A good reconstruction of the input signal shown in Fig. 4(a) has been achieved, despite the fact that the pulses are overlapping. Each constituent pulse has also been successively reconstructed as shown in Figs. 4(b) and (c). Compared with the equivalent results in [33], a significantly improved reconstruction of both $s_1(t)$ and $s_2(t)$, and therefore for the final signal too, is observed. To quantify how well we have been able to reconstruct the input signal, the parameters of the two pulses which were summed to create it, and a comparison with our estimations, are shown in Table 3. The corresponding results as reported in [33] are also shown.

There is a very good match between the parameters estimated by our method and the input parameters for both $s_1(t)$ and $s_2(t)$. It is also evident that our estimated parameters are closer to the true value compared with the estimation of the grid search approach. This is expected since gradient descent is not restricted by the fineness of a grid, but gradually and continuously approaches the true value of the parameter being estimated, since the step taken in every iteration is a function of how close/far the current prediction is from the true value. Again, any small errors in our estimation can be improved by optimising the relevant q value when implementing gradient descent.

In the results presented above, we have examined input signals constructed by summing pulses with different central frequencies. As discussed in Section 2, such pulses generate distinct maxima on a |CT| or a |CWT| plot and it is therefore more straightforward to

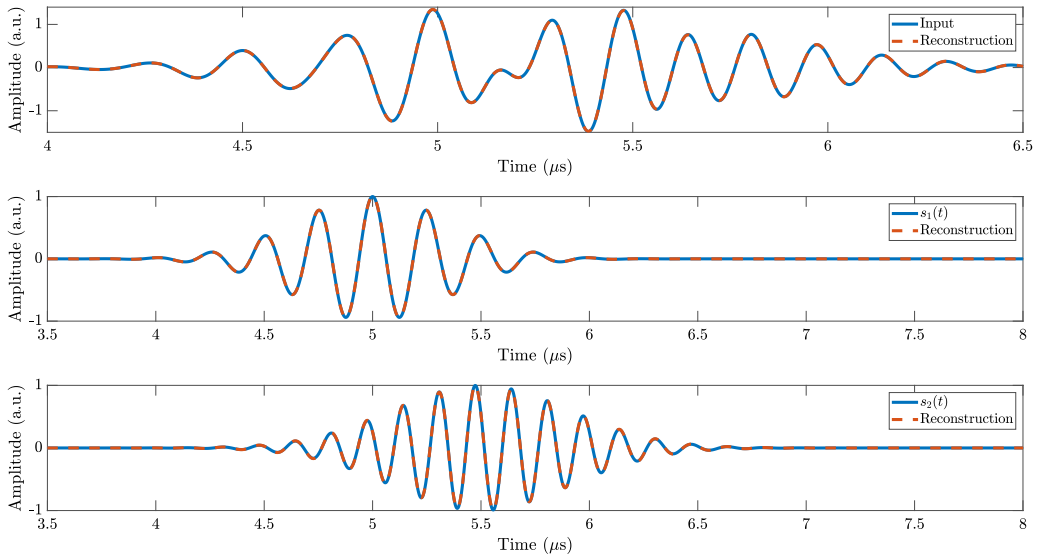


Fig. 4. Example of an input signal, comprising of two overlapping pulses (with different central frequencies) and its reconstructions (a). In (b) and (c) the result of the first and second iteration of the reconstruction process are plotted respectively, as well as a comparison with the corresponding pulses which were used to generate the signal shown in (a).

Table 3
Comparison between the input and estimated parameters of the signals shown in Fig. 4.

Parameter	A	τ	f	α	ϕ
Input parameters $[s_1(t)]$	1	5	4	4	0
Estimated parameters $[s_1(t)]$	1.00	5.00	4.00	4.00	0.01
Estimated parameters $[s_1(t)]$ from [33]	0.997	5.00	4.00	4.10	0.00
Input parameters $[s_2(t)]$	1	5.5	6	3	1
Estimated parameters $[s_2(t)]$	1.00	5.50	6.00	3.04	0.99
Estimated parameters $[s_2(t)]$ from [33]	1.1032	5.52	5.95	3.00	1.80

proceed with the estimation process. When signals contain pulses with the same (or very similar) central frequencies, the maxima overlap and the estimation process becomes more complicated, as it is possible that the maximum of the |CT| or the |CWT| which is used for estimating τ, f and A (or τ_c, f_c and A_c respectively) does not correspond to any of those pulses, due to constructive interference of the maxima. The authors in [33,35] mitigate this by suitable windowing of the |CT|, but acknowledge that this becomes increasingly difficult for strongly overlapping pulses.

We assessed the performance of our method for this more challenging case too — Fig. 5 shows two examples comprising four and six pulses, with the same central frequency, arranged in a strongly overlapping configuration. Despite the overlap, our method is able to recreate the input signals very accurately, regardless of the number of pulses used to create them or the degree of overlap between the pulses.

Since we are using a gradient descent approach, the effect of any erroneous initial predictions of τ and f (or τ_c and f_c) resulting from strongly overlapping pulses diminishes during the gradient descent process. Additionally, our choice to predict A (or A_c) last in the parameter estimation process, and not as a function of the |CWT| (or the |CT|) prohibits any overlap in the maxima in the |CWT| (or the |CT|) from affecting the prediction of the amplitude. The amplitude predictions becomes solely a function of minimising the L_2 norm, i.e. the chosen A (or A_c) yields maximum similarity between $y(t)$ and $s_m(t)$ or $c_m(t)$.

3.3. Realistic signals

In this final section of the results, we are considering two types of realistic signals. In the first case, a signal obtained from FE modelling was reconstructed. The FE domain solved comprised a two dimensional plate, with a notch at the bottom boundary. The notch was rotated by 5° with respect to the vertical. A single, embedded source node was defined in the model. In FE models, these nodes are assigned pre-determined forcing and are thus used to excite waves in the model. We assigned a 3-cycle Hann windowed toneburst with a central frequency of 2.25 MHz to the source node in this model. The source node was displaced vertically to encourage the excitation of a longitudinal wave in that dicrection, which after reflecting from various geometrical features was received at the same location as where the excitation took place; the location acting simultaneously as a source and a receiver is denoted by the red dot in the figure. While embedded sources are not realistic, they are commonly used in FE

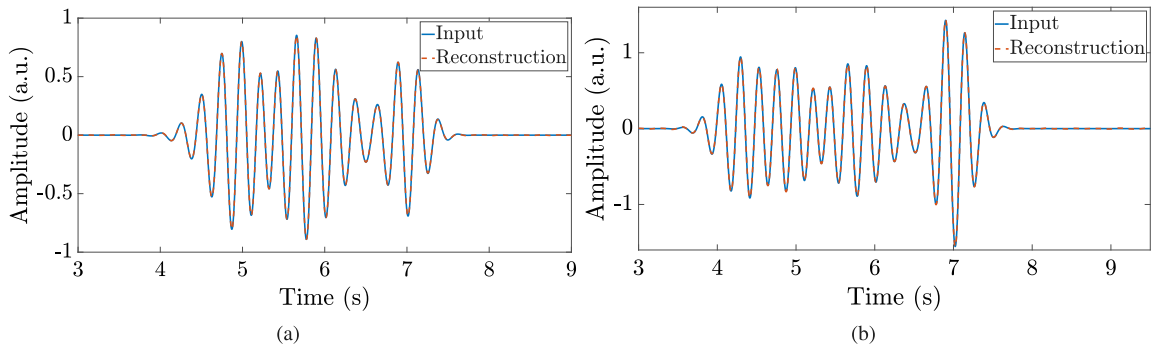


Fig. 5. Examples of input signals, comprising multiple overlapping pulses. In (a), four overlapping pulses were summed to generate the input signal, while in (b) six overlapping pulses were used.

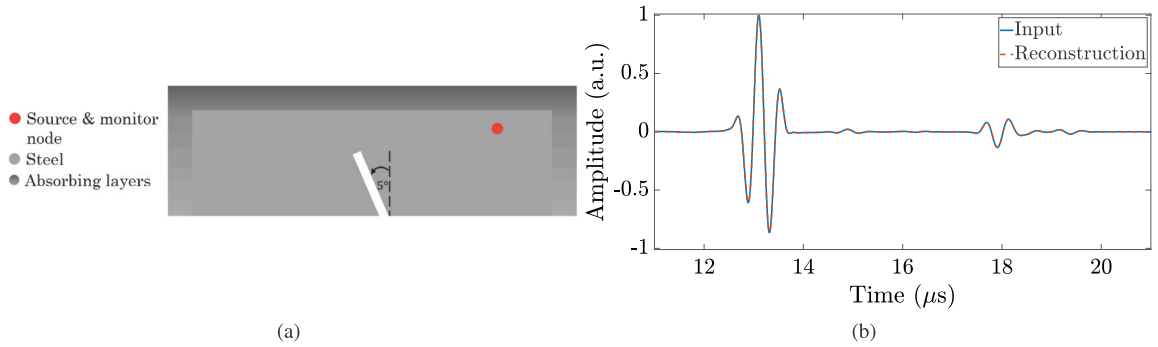


Fig. 6. Example of an FE modelling generated signal, and corresponding reconstruction (b). The schematic of the model from which this signal was generated is shown in (a); details about the model and setup which resulted in this signal are detailed in Section 3.3.

modelling to generate responses with fewer reflections, as they allow ALs to be defined around the surface on which they would have otherwise been defined. Surface waves are also eliminated by this approach; while they can be generated in experiments their amplitudes typically vary significantly depending on exact transducer design, coupling conditions etc. and this approach eliminates this uncertain behaviour. The model was solved using the graphics processing unit accelerated FE solver Pogo [55]. A schematic of the model is shown in Fig. 6(a), and a signal obtained from solving this model is shown in Fig. 6(b).

There are three primary pulses in the signals shown in Fig. 6. The pulse arriving first is a reflection from the bottom surface, the third pulse is a reflection from the face of the notch closest to the monitoring location, while the pulse in the middle is a result of corner trapping — a phenomenon in which the interference of the ultrasound with the two perpendicular edges defining the corner of the crack generates a strong reflection. While it is clear that the three pulses have different characteristics, the reconstruction is still very accurate. This is also despite any noise/low frequency components or other secondary features in the signal, which not only do not hinder the reconstruction process, but they themselves are well reconstructed. It is worth noting that these features are not numerical artifacts, as Pogo has been shown to produce reliable results in many cases [56–59]. It is therefore likely that they are either small-amplitude reflections or coherent noise from multiple scattering and wave-domain interactions.

The second type of signals which we examined were from experimental measurements. First, a signal obtained from experimental measurements was decomposed. This particular signal originated from immersion measurements, during which steel plates were scanned to observe the variation of the longitudinal wave speed in them, in the form of C-scans. Details of the experimental setup can be found in [60,61]. Then, a signal obtained from Rayleigh wave measurements, as detailed in [60], with higher signal-to-noise ratio, was also decomposed. The experimental signals from immersion and surface wave measurements and their reconstructions are shown in Fig. 7(a) and 7(b) respectively. A detail of the same subfigures is shown in (c) and (d) respectively, to highlight the performance of the method presented in this work in handling noise.

It is again clear that we are not only able to reconstruct the main features of this experimental signal, but also any noise, coherent or incoherent, present in it. This is particularly useful for data compression purposes as, even in the presence of noise, we are able to accurately decompose experimental signals; this was a significant challenge for previous, grid-search based methods.

The ability to reconstruct signals like the one presented here is particularly important. All cases examined in this work so far were of analytically generated signals which were noise free, had well defined parameters describing them and whose complexity (if any) arose solely from interference between the pulses comprising them. This is not the case with signals generated by FE modelling or from experimental measurements or signals generated from experimental measurements, as shown in Figs. 6 and 7. In those,

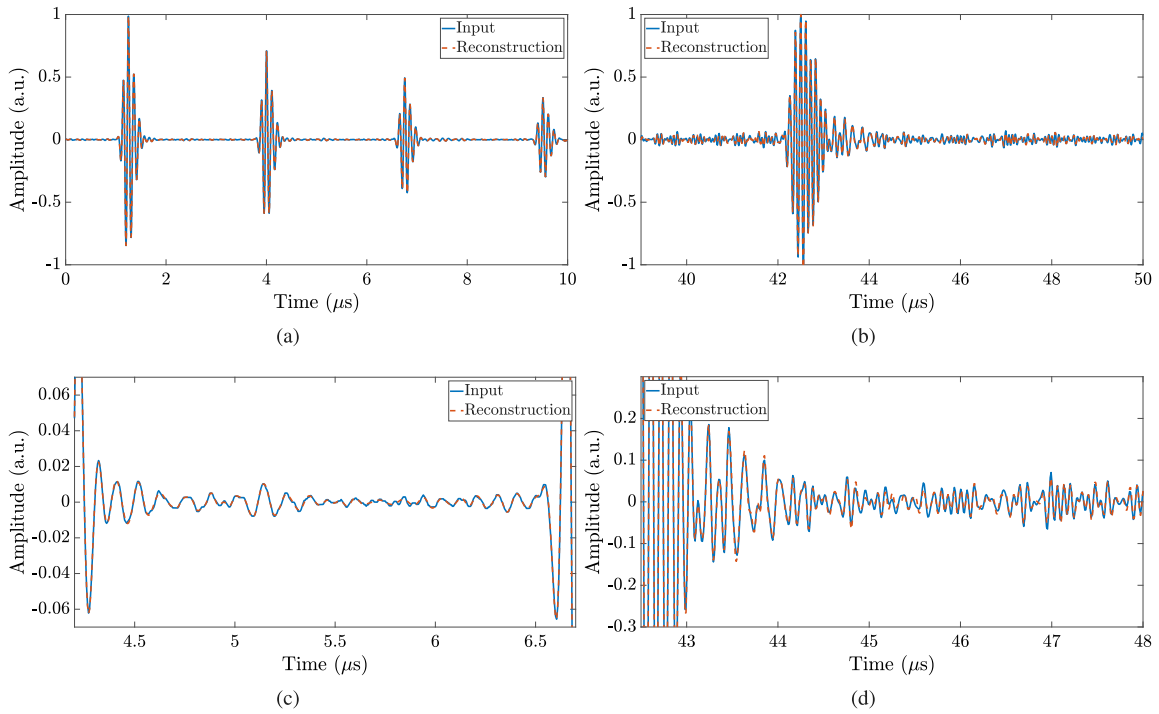


Fig. 7. Examples of signals obtained from experimental measurements and their reconstruction in (a)-(b). In (c) and (d), details of subfigure (a) and (b) are plotted respectively, focusing on the noise existing in the signals.

the shape of the pulses is distorted as a result of the interaction of the input signal with the various geometrical features in the domain/component and where noise, or low amplitude reflections perceived as noise, are also present.

3.4. Data compression & convergence remarks

One of the key motivations of the method is for compressing ultrasonic data. The degree of data compression depends primarily on two factors; the sampling frequency of the signal, which dictates how many datapoints comprise the time trace, and the required reconstruction quality, with the latter being directly linked to the number of iterations undertaken to reach sufficient reconstruction quality.

The signals presented in this work contained approximately 25,000 datapoints. Each decomposition iteration only results into 5 parameters for Gaussian decomposition, and 6 parameters for chirplet decomposition. This means that for a signal comprising a single pulse or chirplet, the data required to fully capture it is 99.98% less compared with its full time domain representation. The data compression benefit reduces with the complexity of the signal, as more iterations are required to decompose it. It is worth noting though that no more than 20 iterations were required for most of the signals presented in this article, which corresponds to a reduction in stored data of 99.92%. Signals comprising a single pulse only required 1 iteration for full reconstruction. The only case requiring more iterations was the decomposition of the experimental signals in Fig. 7. We believe this to be a result of the rapid variations in the amplitude of the noise. If few iterations are used, our method acts as a denoising filter, extracting the main features. If full decomposition is required, more iterations are needed to reach E values equivalent to those of the noise-free signals. In the noisy cases presented here, reconstruction was achieved in no more than 150 iterations.

In terms of convergence of our method, we are providing plots showing the evolution of E as the number of pulses M increases for the cases shown in Figs. 5–7 in Appendix. In all cases, E reduces monotonically, showing that our method is robust and well behaved, regardless of the number of pulses, degree of overlap, origin of the signal (analytical, FE-generated or experimental) and the presence of noise. Plots are not provided for the signals containing a single pulse, or multiple, well separated pulses since those converge as soon as M is equal to the number of pulses in the signal.

4. Conclusion

In this work, we have presented a method able to decompose an ultrasonic signal into sums of simple pulses, and subsequently use these pulses to accurately reconstruct the input signal. This was achieved by modifying and extending a well established MP algorithm, in which the CWT or the CT of a signal is used to successively estimate the parameters of simple pulses in which the signal is decomposed. Our modification involves using a gradient descent assisted approach during the parameter estimation stage,

which allows accurate estimation of each parameter, contrary to more traditional, grid-search approaches which are limited in their accuracy by the fineness of the grid. There are also notable advantages when comparing our method with more recent, machine-learning approaches. Those typically require large, labelled datasets for training, which can be difficult to acquire for many ultrasonic applications, to ensure they perform well in many scenarios. The method proposed in this work, by contrast, is based on analytical, largely closed-form approaches, requires no prior training and is inherently generalisable to pulses other than Gaussians or chirplets if required.

We derived the necessary equations to implement gradient descent in combination with the MP algorithm, both for decomposition into Gaussian pulses and chirps. The method was then initially validated with signals comprising a single pulse; by using those we were able to demonstrate that our method is able to estimate the parameters describing those signals very accurately. Following this validation, examples of increasing complexity were examined, including signals with multiple non-overlapping pulses and signals with multiple, overlapping pulses. For the latter case both signals comprising pulses with different, and the same (or very similar) central frequencies, were examined. In all examples presented, our method was able to reconstruct the input signal accurately, regardless of its level of complexity. Finally, in recognition of the fact that a real-life signal will exhibit additional features, realistic signals from both FE modelling and experiments were considered, demonstrating the ability of this method to perform well with realistic inputs and in the presence of noise, which has previously been a challenge to accurately decompose.

CRediT authorship contribution statement

Georgios Sarris: Writing – review & editing, Writing – original draft, Visualization, Validation, Software, Methodology, Investigation, Formal analysis, Data curation. **Michael J.S. Lowe:** Writing – review & editing, Supervision, Funding acquisition, Conceptualization. **Peter Huthwaite:** Writing – review & editing, Supervision, Software, Resources, Project administration, Funding acquisition, Conceptualization.

Declaration of competing interest

The authors declare the following financial interests/personal relationships which may be considered as potential competing interests: Georgios Sarris, Michael J. S. Lowe, Peter Huthwaite reports financial support was provided by UK Research and Innovation. If there are other authors, they declare that they have no known competing financial interests or personal relationships that could have appeared to influence the work reported in this paper.

Acknowledgements

The authors are funded by UK Research and Innovation, United Kingdom – Project reference EP/X02427X/1.

Appendix

In this section, we present how we arrived at the expressions in Eqs. (10)–(13) and in Eqs. (24)–(28). First, we present the relevant theory regarding derivates of the absolute value of complex valued functions, and apply it to Eqs. (10)–(12) and Eqs. (24)–(27). Then, after a short remark on how to cater for the $\{\cdot\}^*$ operation (which is applicable to all derivative terms calculated here), and the $\mathfrak{R}\{\cdot\}$ operation, we calculate the derivative terms in Eqs. (13) and (28). In the last subsection of the Appendix, we present plots showing the evolution of E as M increases for cases were complicates signals containing multiple overlapping pulses and/or noise were decomposed in this work.

A.1. Derivative of the magnitude of a complex valued function

A.1.1. Theory

Let us consider a function $g(x_1, x_2, \dots, x_n)$, with $g : \mathbb{R}^n \to \mathbb{C}$. We can express g as

$$g(x_1, x_2, \dots, x_n) = u(x_1, x_2, \dots, x_n) + iv(x_1, x_2, \dots, x_n),$$

with

$$u(x_1, x_2, \dots, x_n) = \mathfrak{R}\{g(x_1, x_2, \dots, x_n)\},$$

and

$$v(x_1, x_2, \dots, x_n) = \mathfrak{I}\{g(x_1, x_2, \dots, x_n)\},$$

where $\mathfrak{R}\{\cdot\}$ and $\mathfrak{I}\{\cdot\}$ denote the real and imaginary part of the argument respectively. For brevity, $g(x_1, x_2, \dots, x_n)$, $u(x_1, x_2, \dots, x_n)$ and $v(x_1, x_2, \dots, x_n)$ will be denoted as g, u and v respectively.

Let us start by calculating $|g|$. This is given by

$$|g| = \sqrt{u^2 + v^2}.$$

The derivative of $|g|$ with respect to any variable, x_k, with $k = 1, 2 \dots n$ is given from:

$$\frac{\partial |g|}{\partial x_k} = \frac{u\frac{\partial u}{\partial x_k} + v\frac{\partial v}{\partial x_k}}{\sqrt{u^2+v^2}}. \tag{A.1}$$

Also, the derivative of g with respect to any variable, x_k, with $k = 1, 2 \dots n$ is simply given from

$$\frac{\partial g}{\partial x_k} = \frac{\partial u}{\partial x_k} + i\frac{\partial v}{\partial x_k}. \tag{A.2}$$

Let us now evaluate the expression $\frac{|g|}{g}$:

$$\frac{|g|}{g} = \frac{\sqrt{u^2+v^2}}{u+iv} = \frac{\sqrt{u^2+v^2}}{u+iv}\frac{u-iv}{u-iv} = (u-iv)\frac{\sqrt{u^2+v^2}}{u^2+v^2} = \frac{u-iv}{\sqrt{u^2+v^2}}. \tag{A.3}$$

Multiplying Eqs. (A.2) and (A.3) yields

$$\frac{|g|}{g}\frac{\partial g}{\partial x_k} = \frac{u-iv}{\sqrt{u^2+v^2}}\left(\frac{\partial u}{\partial x_k} + i\frac{\partial v}{\partial x_k}\right). \tag{A.4}$$

Now, the real part of Eq. (A.4) is given from

$$\Re\left\{\frac{|g|}{g}\frac{\partial g}{\partial x_k}\right\} = \frac{u\frac{\partial u}{\partial x_k} + v\frac{\partial v}{\partial x_k}}{\sqrt{u^2+v^2}}, \tag{A.5}$$

which is the same expression as Eq. (A.1). Therefore,

$$\frac{\partial |g|}{\partial x_k} = \Re\left\{\frac{|g|}{g}\frac{\partial g}{\partial x_k}\right\}. \tag{A.6}$$

A.1.2. Application to the decomposition into Gaussian pulses

Eq. (A.6) can now be applied to Eqs. (6)–(8) as follows:

$$\frac{\partial |\mathrm{CWT}|}{\partial b} = \Re\left\{\frac{|\mathrm{CWT}|}{\mathrm{CWT}}\int_{-\infty}^{\infty} s(t)\frac{\partial \psi^*(t)}{\partial b}dt\right\}, \tag{A.7}$$

$$\frac{\partial |\mathrm{CWT}|}{\partial f_0} = \Re\left\{\frac{|\mathrm{CWT}|}{\mathrm{CWT}}\int_{-\infty}^{\infty} s(t)\frac{\partial \psi^*(t)}{\partial f_0}dt\right\}, \tag{A.8}$$

$$\frac{\partial |\mathrm{CWT}|}{\partial \gamma} = \Re\left\{\frac{|\mathrm{CWT}|}{\mathrm{CWT}}\int_{-\infty}^{\infty} s(t)\frac{\partial \psi^*(t)}{\partial \gamma}dt\right\}. \tag{A.9}$$

The equations above involve the differentiating the conjugate of $\psi(t)$ — a remark regarding how to treat this is presented in the next subsection.

The derivatives of $\psi(t)$ are given by:

$$\frac{\partial \psi(t)}{\partial b} = [2\gamma(t-b) - 2\pi i f_0]\psi(t), \tag{A.10}$$

$$\frac{\partial \psi(t)}{\partial f_0} = 2\pi i(t-b)\psi(t), \tag{A.11}$$

$$\frac{\partial \psi(t)}{\partial \gamma} = \left[\frac{1}{4\gamma} - (t-b)^2\right]\psi(t). \tag{A.12}$$

A.1.3. Application to the decomposition into chirplets

Eq. (A.6) can also be applied to Eqs. (19)–(22) as follows:

$$\frac{\partial |\mathrm{CT}|}{\partial b_c} = \Re\left\{\frac{|\mathrm{CT}|}{\mathrm{CT}}\int_{-\infty}^{\infty} s(t)\frac{\partial \chi^*(t)}{\partial b_c}dt\right\}, \tag{A.13}$$

$$\frac{\partial |\mathrm{CT}|}{\partial f_{0_c}} = \Re\left\{\frac{|\mathrm{CT}|}{\mathrm{CT}}\int_{-\infty}^{\infty} s(t)\frac{\partial \chi^*(t)}{\partial f_{0_c}}dt\right\}, \tag{A.14}$$

$$\frac{\partial |\mathrm{CT}|}{\partial \gamma_1} = \Re\left\{\frac{|\mathrm{CT}|}{\mathrm{CT}}\int_{-\infty}^{\infty} s(t)\frac{\partial \chi^*(t)}{\partial \gamma_1}dt\right\}. \tag{A.15}$$

$$\frac{\partial |\mathrm{CT}|}{\partial \gamma_2} = \Re\left\{\frac{|\mathrm{CT}|}{\mathrm{CT}}\int_{-\infty}^{\infty} s(t)\frac{\partial \chi^*(t)}{\partial \gamma_2}dt\right\}. \tag{A.16}$$

with the derivatives of $\chi(t)$ being given by:

$$\frac{\partial \chi(t)}{\partial b_c} = 2[\gamma_1(t-b_c) - i\pi f_{0_c} + \gamma_2(t-b_c)]\chi(t), \tag{A.17}$$

$$\frac{\partial \chi(t)}{\partial f_{0_c}} = 2\pi i(t-b_c)\chi(t), \tag{A.18}$$

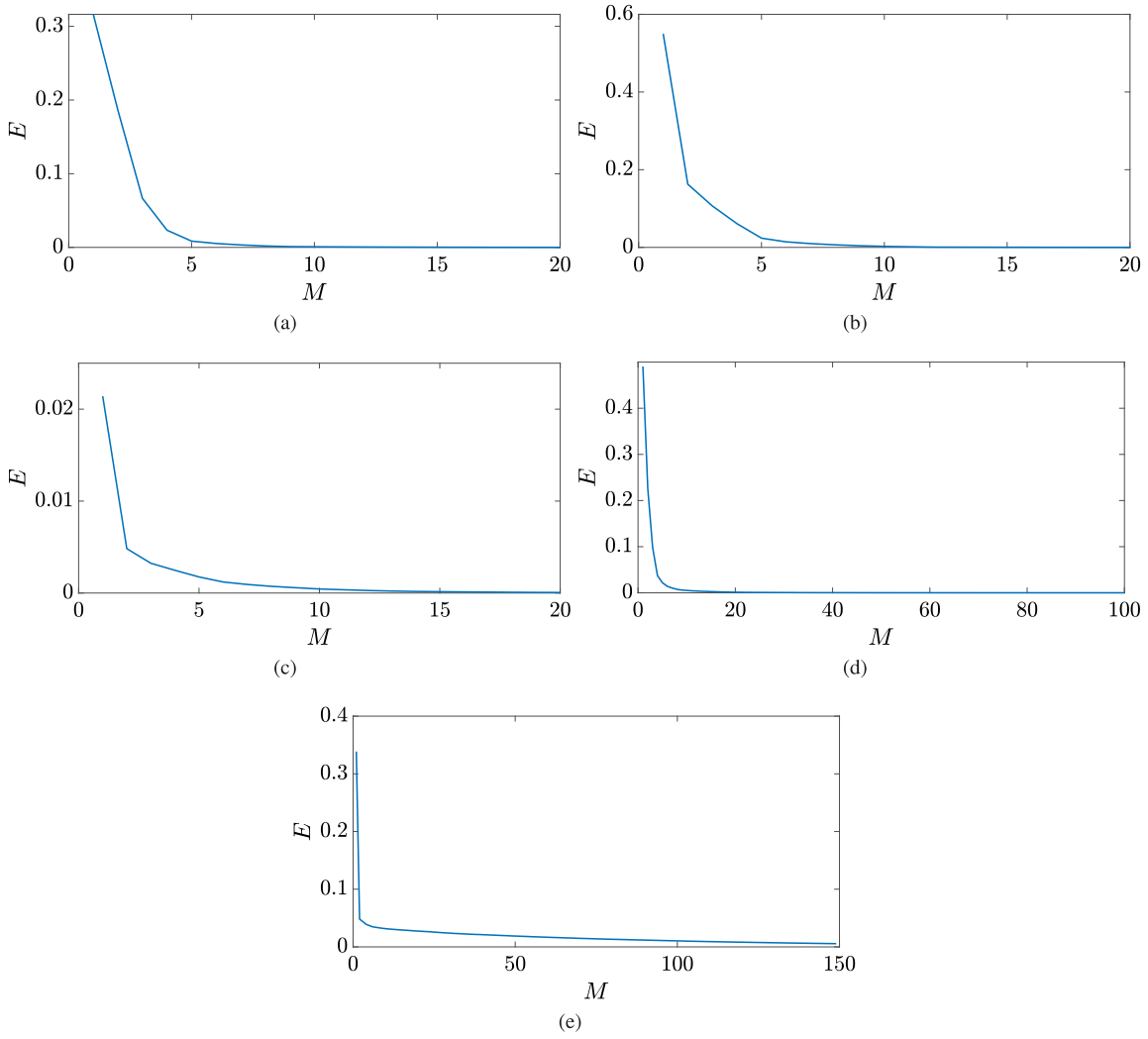


Fig. 8. Evolution of the relative energy threshold, E as the number of iterations, and hence pulses to which the input signal is being decomposed to, M increases. Subfigures (a)–(e) correspond to the variation of E as M increases for the signals shown in Figs. 5(a), 5(b), 6(b), 7(a) and 7(b) respectively.

$$\frac{\partial \chi(t)}{\partial \gamma_2} = i(t - b_c)^2 \chi(t) \tag{A.19}$$

$$\frac{\partial \chi(t)}{\partial \gamma_1} = \left[\frac{1}{4\gamma} - (t - b_c)^2\right] \chi(t) \tag{A.20}$$

A.2. Derivative of the conjugate and the real part of a complex valued function

In many equations presented in the manuscript, it is necessary to take the derivative of the complex conjugate of a complex-valued function, or the derivative of the real part of that function. Due to the linearity of both the $\{\cdot\}^*$ and the $\Re\{\cdot\}$ operations, it is straightforward to show that

$$\frac{\partial g^*}{\partial x_k} = \left\{\frac{\partial g}{\partial x_k}\right\}^*. \tag{A.21}$$

and

$$\frac{\partial \Re\{g\}}{\partial x_k} = \Re\left\{\frac{\partial g}{\partial x_k}\right\}. \tag{A.22}$$

Eq. (A.21) is useful for evaluating all the derivatives involving $\psi^*(t)$ and $\chi^*(t)$, as one can simply use the conjugate of the expressions in Eqs. (A.10)–(A.12) and (A.17)–(A.20).

Finally, Eq. (A.22) above can be applied to Eqs. (9) and (23) as follows:

$$\frac{\partial \Re\{\mathrm{CWT}\}}{\partial \theta} = \Re\left\{\int_{-\infty}^{\infty} s(t)\frac{\partial \psi^*(t)}{\partial \theta}dt\right\}, \tag{A.23}$$

$$\frac{\partial \Re\{\mathrm{CT}\}}{\partial \theta} = \Re\left\{\int_{-\infty}^{\infty} s(t)\frac{\partial\ \chi^*(t)}{\partial \theta}dt\right\} \tag{A.24}$$

with

$$\frac{\partial \psi(t)}{\partial \theta} = i\psi(t), \tag{A.25}$$

and

$$\frac{\partial\ \chi(t)}{\partial \theta} = i\chi(t). \tag{A.26}$$

A.3. Error evolution plots

In Fig. 8 we are plotting the evolution of the relative energy threshold E, defined in Step 5 of the decomposition process described in Section 2. This was used as metric to quantify how close the reconstructed signal is to the input. A value of zero denotes perfect reconstruction, as it implies that $r(t)$, the remainder at the latest iteration, has reached zero energy.

In all cases robust, monotonic convergence is observed. This is regardless of the origin of the signal (analytical, FE-generated or experimental), the number of pulses comprising and the presence of noise. It is worth noting that even though the signals to which the results in (a) and (b) here correspond to comprise 4 and 6 pulses respectively, we require more pulses to fully decompose them. This is due to the lack of a non-unique sum of pulses defining these signals, as the central frequency of the pulses comprising them is the same.

Data availability

Data will be made available on request.

References

[1] Richard E. Challis, Richard J. Freemantle, G.P Wilkinson, J.D.H White, Compression wave NDE of adhered metal lap joints: uncertainties and echo feature extraction, Ultrasonics 34 (2–5) (1996) 315–319.

[2] E.M. Severin, R. Gr Maev, Adaptive filtration of ultrasonic signals in the evaluation of adhesive bonds in automotive bodies, Insight - Non-Destructive Test. Cond. Monit. 47 (1) (2005) 8–10.

[3] Mehdi Hajian, Farhang Honarvar, Reflectivity estimation using an expectation maximization algorithm for ultrasonic testing of adhesive bonds, Mater. Eval. 69 (2) (2011) 208–219.

[4] Pan Dou, Peng Zheng, Yaping Jia, Tonghai Wu, Min Yu, Tom Reddyhoff, Wei-Hsin Liao, Zhongxiao Peng, Ultrasonic measurement of oil film thickness in a four-layer structure for applications including sliding bearings with a thin coating, NDT & E Int. 131 (2022) 102684.

[5] Peng Zheng, Pan Dou, Quanzhong Wu, Yaping Jia, Tonghai Wu, Min Yu, Yaguo Lei, Tom Reddyhoff, Ultrasonic reflection measured oil film thickness in the slipper bearings of an aviation fuel piston pump, Mech. Syst. Signal Process. 220 (2024) 111696–111696.

[6] Kai Zhang, Tonghai Wu, Zhihe Duan, Qingfeng Meng, Qinghu Meng, An adaptive approach for recovering overlapping echoes in oil film thickness measurement by ultrasound, Ind. Lubr. Tribol. 69 (5) (2017) 788–797.

[7] Shaorui Fan, Maodan Yuan, Jianlin Xu, Yongfeng Song, Yan Chen, Xuanrong Ji, Nondestructive evaluation of bonding quality of dual-layer coatings based on the multi-feature ultrasonic method, Appl. Acoust. 224 (2024) 110151–110151.

[8] James B. Robinson, Rhodri E. Owen, Matt D.R. Kok, Maximilian Maier, Jude Majasan, Michele Braglia, Richard Stocker, Tazdin Amietszajew, Alexander J. Roberts, Rohit Bhagat, Duncan Billsson, Jarred Z. Olson, Juyeon Park, Gareth Hinds, Annika Ahlberg Tidblad, Dan J.L. Brett, Paul R. Shearing, Identifying defects in li-ion cells using ultrasound acoustic measurements, J. Electrochem. Soc. 167 (12) (2020) 120530.

[9] Wenhua Zuo, Rui Liu, Jiyu Cai, Yonggang Hu, Manar Almazrouei, Xiangsi Liu, Tony Cui, Xin Jia, Emory Apodaca, Jakob Alami, Zonghai Chen, Tianyi Li, Wenqian Xu, Xianghui Xiao, Dilworth Parkinson, Yong Yang, Gui-Liang Xu, Khalil Amine, Nondestructive analysis of commercial batteries, Chem. Rev. 125 (2024).

[10] Matthew R. Webster, Erik L. Frankforter, Peter Juarez, Evaluation of ultrasonic battery inspection techniques, Nondestruct. Charact. Monit. Adv. Mater. Aerosp. Civ. Infrastruct. Transp. XVII 12487 (2023).

[11] Yi Wu, Youren Wang, Winco K.C. Yung, Michael Pecht, Ultrasonic health monitoring of lithium-ion batteries, Electronics 8 (7) (2019) 751.

[12] Ming Huang, Niall Kirkaldy, Yan Zhao, Yatish Patel, Frederic Cegla, Bo Lan, Quantitative characterisation of the layered structure within lithium-ion batteries using ultrasonic resonance, J. Energy Storage 50 (2022) 104585.

[13] Abdessalem Benammar, Redouane Drai, Abderrezak Guessoum, Detection of delamination defects in CFRP materials using ultrasonic signal processing, Ultrasonics 48 (8) (2008) 731–738.

[14] Ivan Pelivanov, Lukasz Ambroziński, Anton Khomenko, Ermias G. Koricho, Gary L. Cloud, Mahmoodul Haq, Matthew O'Donnell, High resolution imaging of impacted CFRP composites with a fiber-optic laser-ultrasound scanner, Photoacoustics 4 (2) (2016) 55–64.

[15] Alberto Rodríguez-Martínez, Linas I. Svilainis, Vytautas I. Dumbrava, Andrius Chaziachmetovas, Addison Salazar, Automatic simultaneous measurement of phase velocity and thickness in composite plates using iterative deconvolution, NDT & E Int. 66 (2014) 117–127.

[16] Yong Chang, Yanyang Zi, Jiyuan Zhao, Zhe Yang, Wangpeng He, Hailiang Sun, An adaptive sparse deconvolution method for distinguishing the overlapping echoes of ultrasonic guided waves for pipeline crack inspection, Meas. Sci. Technol. 28 (3) (2017) 035002–035002.

[17] Houman Nakhli Mahal, Kai Yang, Asoke K. Nandi, Defect detection using power spectrum of torsional waves in guided-wave inspection of pipelines, Appl. Sci. 9 (7) (2019) 1449–1449.

[18] Yong Chang, Nana Li, Jiyuan Zhao, Yu Wang, Zhe Yang, A novel ultrasonic guided wave-based method for railway contact wire defect detection, IEEE Trans. Instrum. Meas. 71 (2022) 1–9.
[19] Jianjun Wu, Zhifeng Tang, Fuzai Lv, Keji Yang, Chung Bang Yun, Yuanfeng Duan, Ultrasonic guided wave-based switch rail monitoring using independent component analysis, Meas. Sci. Technol. 29 (11) (2018) 115102–115102.
[20] Da-Zhi Dang, You-Wu Wang, Yi-Qing Ni, A novel guided wave testing method for identifying rail web cracks using optical fiber bragg grating sensing and orthogonal matching pursuit, Measurement 243 (2024) 116317–116317.
[21] Jiadong Hua, Broadband sparse decomposition of lamb wave signals, J. Nondestruct. Eval. 42 (3) (2023).
[22] Hongbo Jia, Zhichun Zhang, Hongwei Liu, Fuhong Dai, Yanju Liu, Jinsong Leng, An approach based on expectation-maximization algorithm for parameter estimation of lamb wave signals, Mech. Syst. Signal Process. 120 (2019) 341–355.
[23] Linda L. Fellingham, Sommer F. Graham, Ultrasonic characterization of tissue structure in the in vivo human liver and spleen, IEEE Trans. Sonics Ultrason. 4 (1984) 418–428.
[24] Edo Bagus Prastika, Atsushi Atsushi Imori, Tomohiro Kawashima, Yoshinobu Murakami, Naohiro Hozumi, Sachiko Yoshida, Ryo Nagaoka, Kazuto Kobayashi, Acoustic impedance interpretation of cross-sectional human skin by using time and frequency domain deconvolution, Japan. J. Appl. Phys. 59 (SK) (2020) SKKB06–SKKB06.
[25] Jean-Gabriel Minonzio, Chao Han, Didier Cassereau, Quentin Grimal, In vivo pulse-echo measurement of apparent broadband attenuation and Q factor in cortical bone: a preliminary study, Phys. Med. Biol. 66 (15) (2021) 155002–155002.
[26] John Wikstrand, Methodological considerations of ultrasound measurement of carotid artery intima2013media thickness and lumen diameter, Clin. Physiol. Funct. Imaging 27 (6) (2007) 341–345.
[27] Shane Steinberg, Continuous Artery Monitoring Based on Decomposition of Ultrasound Radiofrequency Signals (Ph.D. thesis), Carleton University, 2021.
[28] Andy Huang, Masayoshi Yoshida, Yuu Ono, Sreeraman Rajan, Continuous measurement of arterial diameter using wearable and flexible ultrasonic sensor, in: 2017 IEEE International Ultrasonics Symposium, IUS, 2017, pp. 1–4.
[29] Amir Semnani, Liang Wang, Mehdi Ostadhassan, Majid Nabi-Bidhendi, Babak Nadjar Araabi, Time2010frequency decomposition of seismic signals via quantum swarm evolutionary matching pursuit, Geophys. Prospect. 67 (7) (2019) 1701–1719.
[30] Weiqiang Zhu, S. Mostafa Mousavi, Gregory C. Beroza, Seismic signal denoising and decomposition using deep neural networks, IEEE Trans. Geosci. Remote Sens. 57 (11) (2019) 9476–9488.
[31] Tao Lu, Fanqianhui Yu, Jinrui Wang, Xiaoyu Wang, Amith Mudugamuwa, Yanfeng Wang, Baokun Han, Application of adaptive complementary ensemble local mean decomposition in underwater acoustic signal processing, Appl. Acoust. 178 (2021) 107966.
[32] Ramazan Demirli, Jafar Saniie, Model-based estimation of ultrasonic echoes. Part I: Analysis and algorithms, IEEE Trans. Ultrason. Ferroelectr. Freq. Control 48 (3) (2001) 787–802.
[33] Guilherme Cardoso, Jafar Saniie, Ultrasonic data compression via parameter estimation, IEEE Trans. Ultrason. Ferroelectr. Freq. Control 52 (2) (2005) 313–325.
[34] Florian Boßmann, Gerlind Plonka, Thomas Peter, Oliver Nemitz, T. Schmitte, Sparse deconvolution methods for ultrasonic NDT, J. Nondestruct. Eval. 31 (3) (2012) 225–244.
[35] Yufeng Lu, Ramazan Demirli, Guilherme Cardoso, Jafar Saniie, A successive parameter estimation algorithm for chirplet signal decomposition, IEEE Trans. Ultrason. Ferroelectr. Freq. Control 53 (11) (2006) 2121–2131.
[36] Yufeng Lu, Erdal Oruklu, Jafar Saniie, Chirplet signal and empirical mode decompositions of ultrasonic signals for echo detection and estimation, J. Signal Inf. Process. 04 (02) (2013) 149–157.
[37] Roberto Henry Herrera, Rubén Orozco, Manuel Rodriguez, Wavelet-based deconvolution of ultrasonic signals in nondestructive evaluation, J. Zhejiang Univ. Sci. A 7 (10) (2006) 1748–1756.
[38] Kristina Lukoseviciute, Migle Drulyte, Linas Svilainis, Approximation performance of model functions for blind deconvolution of ultrasonic reflections, J. Vibroengineering 18 (4) (2016) 2563–2573.
[39] Meng Lian, Haibo Liu, Qile Bo, Tongyu Zhang, Te Li, Yongqing Wang, An improved matching pursuit method for overlapping echo separation in ultrasonic thickness measurement, Meas. Sci. Technol. 30 (6) (2019) 065001–065001.
[40] Jim Leinbach, Wiener spiking deconvolution and minimum2010phase wavelets: A tutorial, Lead. Edge 14 (3) (1995) 189–192.
[41] Tindaro Cicero, Signal Processing for Guided Wave Structural Health Monitoring (Ph.D. thesis), Imperial College London, 2009.
[42] Emma Wilson, Thomas M Conneely, Andrey Mudrov, Ivan Tyukin, Implementation of the prony method for signal deconvolution, IFAC-PapersOnLine 52 (29) (2019) 269–273.
[43] Dongxun Li, Zhaoqi Chen, Yulong Zhang, Sheng Zhao, Wangyu Liu, Separation of multi-echo overlapping ultrasonic signals for increasing the axial resolution using a neural network, Meas. Sci. Technol. 34 (12) (2023) 125009–125009.
[44] Zhaoxu Lu, Kai Yao, Xinglong Li, Chenghao Yu, Research on ultrasonic defect imaging based on a neural network with Gaussian weight function fusion model, Constr. Build. Mater. 411 (2023) 134229–134229.
[45] Pramod Govindan, Boyang Wang, Prashaanth Ravi, Jafar Saniie, Hardware and software architectures for computationally efficient three2010dimensional ultrasonic data compression, IET Circuits, Devices & Syst. (Print) 10 (1) (2016) 54–61.
[46] Boyang Wang, Jafar Saniie, Massive ultrasonic data compression using wavelet packet transformation optimized by convolutional autoencoders, IEEE Trans. Neural Networks Learn. Syst. 34 (3) (2021) 1–11.
[47] None Jin-Chul Hong, Kyung Ho, Young Kim, Waveguide damage detection by the matching pursuit approach employing the dispersion-based chirp functions, IEEE Trans. Ultrason. Ferroelectr. Freq. Control. 53 (3) (2006) 592–605.
[48] J. Mamou, J.A. Ketterling, R.H. Silverman, Chirp-coded excitation imaging with a high-frequency ultrasound annular array, IEEE Trans. Ultrason. Ferroelectr. Freq. Control 55 (2) (2008) 508–513.
[49] Orlando Arsitizabal, Daniel H. Turnbull, Jonathan Mamou, Jeffrey A. Ketterling, 40 MHz annular-array in utero imaging of mouse embryos with chirp coded excitation, in: 2008 IEEE Ultrasonics Symposium, 2008, pp. 126–129.
[50] Kim L. Blackmore, Robert C. Williamson, Local minima and attractors at infinity for gradient descent learning algorithms, J. Math. Syst. Estim. Control. 6 (2) (1996).
[51] Joan L. Brierton, Techniques for avoiding local minima in gradient-descent-based ID algorithms, Proc. SPIE, Int. Soc. Opt. Engineering/Proceedings SPIE 3066 (1997) 130–135.
[52] Michael R. Frater, Robert R. Bitmead, C. Richard Johnson, Local minima escape transients by stochastic gradient descent algorithms in blind adaptive equalizers, Automatica 31 (4) (1995) 637–641.
[53] Mathew M. Noel, A new gradient based particle swarm optimization algorithm for accurate computation of global minimum, Appl. Soft Comput. 12 (1) (2012) 353–359.
[54] Bin Shi, Sundaraja S. Iyengar, Mathematical Theories of Machine Learning - Theory and Applications, Springer Nature, 2020, Springer EBooks.
[55] Peter Huthwaite, Accelerated finite element elastodynamic simulations using the GPU, J. Comput. Phys. 257 (2014) 687–707.
[56] Georgios Sarris, Stewart G. Haslinger, Peter Huthwaite, Peter B. Nagy, Michael J.S. Lowe, Attenuation of Rayleigh waves due to three-dimensional surface roughness: A comprehensive numerical evaluation, J. Acoust. Soc. Am. 154 (2) (2023) 808–818.
[57] Panpan Xu, Robin Jones, Georgios Sarris, Peter Huthwaite, Efficient generation of realistic guided wave signals for reliability estimation, Struct. Health Monit. (2025).

[58] Stewart G. Haslinger, Michael J.S. Lowe, Peter Huthwaite, Richard V. Craster, Fan Shi, Appraising Kirchhoff approximation theory for the scattering of elastic shear waves by randomly rough defects, J. Sound Vib. 460 (2019) 114872.
[59] Filip Szlaszynski, Michael J.S. Lowe, Peter Huthwaite, Short range pipe guided wave testing using SH0 plane wave imaging for improved quantification accuracy, Sensors 22 (8) (2022) 2973.
[60] Georgios Sarris, Stewart G. Haslinger, Peter Huthwaite, Michael J.S. Lowe, Ultrasonic methods for the detection of near surface fatigue damage, NDT & E Int. 135 (2023) 102790.
[61] Georgios Sarris, Stewart G. Haslinger, Peter Huthwaite, Michael, Fatigue state characterization of steel pipes using ultrasonic shear waves, IEEE Trans. Ultrason. Ferroelectr. Freq. Control. 70 (1) (2022) 72–80.